Conf-911106--33

3D Image Reconstruction for PET by Multi-Slice Rebinning and Axial Filtering

Robert M. Lewitt[1,2], Gerd Muehllehner[1], and Joel S. Karp[2]

[1]UGM Medical Systems, Inc., 3401 Market St., Suite 222, Philadelphia, PA 19104, and
[2]University of Pennsylvania, Dept. of Radiology, 419 Blockley Hall, Philadelphia, PA 19104–6021.

CONF-911106--33

DE92 003943

Address for Correspondence:

Robert M. Lewitt

Department of Radiology

University of Pennsylvania

419 Blockley Hall

418 Service Drive

Philadelphia, PA 19104–6021

USA

Phone (215) 662–6780

E-mail (Internet) robert@rob.mipg.upenn.edu

Submitted to the Conference Record of the 1991

IEEE Nuclear Science Symposium

Santa Fe, New Mexico, November 1991.

FG02-88ER60642

final 11/15

3D Image Reconstruction for PET by Multi-Slice Rebinning and Axial Filtering

Robert M. Lewitt[1,2], Gerd Muehllehner[1], and Joel S. Karp[2]

[1]UGM Medical Systems, Inc., 3401 Market St., Suite 222, Philadelphia, PA 19104, and
[2]University of Pennsylvania, Dept. of Radiology, 419 Blockley Hall, Philadelphia, PA 19104–6021.

Abstract

Two different approaches are used at present to reconstruct from 3D coincidence data in PET. We refer to these approaches as the single-slice rebinning approach and the fully-3D approach. The single-slice rebinning approach involves geometrical approximations, but it requires the least possible amount of computation. Fully–3D reconstruction algorithms, both iterative and non-iterative, do not make such approximations, but require much more computation. Multi-slice rebinning with axial filtering is a new approach which attempts to achieve the geometrical accuracy of the fully-3D approach with the simplicity and modest amount of computation of the single-slice rebinning approach. The first step (multi-slice rebinning) involves rebinning of coincidence lines into a stack of 2D sinograms, where multiple sinograms are incremented for each oblique coincidence line. This operation is followed by an axial filtering operation, either before or after slice-by-slice reconstruction, to reduce the blurring in the axial direction. Tests with simulated and experimental data indicate that the new method has better geometrical accuracy than single-slice rebinning, at the cost of only a modest increase in computation.

I. INTRODUCTION

Current scanners for positron emission tomography (PET) are now using detector systems that have good spatial resolution in both the transverse and the axial directions, and the axial field of view of the detectors has been increasing steadily. Such detector systems can identify a very large number of different coincidence lines (also known as lines of response) through the three-dimensional (3D) space between opposing detector modules.

For scanners such as the PENN-PET [1–3] that do not use septa to constrain the coincidence lines to be perpendicular to the scanner axis, the lines are oblique for most detected photon pairs and reconstruction algorithms must be devised to handle the fully-3D raw data from the detector system. At present, there are two different approaches that have been used to reconstruct from this data. We refer to these approaches as the *single-slice rebinning* approach and the *fully-3D* approach. The single-slice rebinning approach assigns each oblique coincidence line to a particular 2D sinogram associated with a transverse slice of the volume. The reconstruction of the stack of sinograms proceeds in a slice-by-slice fashion using conventional 2D algorithms. This approach involves geometrical approximations [4], but it requires the least possible amount of computation. Fully–3D reconstruction algorithms, both iterative and non-iterative, process oblique coincidence lines without making geometrical approximations, but image reconstruction using either kind of fully-3D algorithm requires a considerable amount of computation. We do not discuss the fully-3D approach further in this paper, but we refer instead to several recent papers [5–7] that describe applications of this approach to PET and which contain references to earlier work.

We have recently developed an alternative approach to image reconstruction from 3D coincidence data which is intermediate between the approaches already described. It is an attempt to achieve the geometrical accuracy of the fully-3D approach with the simplicity and modest amount of computation of the single-slice rebinning approach. The new approach involves *multi-slice rebinning* of the coincidence lines into a stack of 2D sinograms and an *axial filtering* operation, which can be done either before or after the operation of slice-by-slice reconstruction.

In the method of multi-slice rebinning, multiple sinograms are incremented for each oblique coincidence line. For each oblique coincidence line, the set of transverse slices that it intersects is identified, and each of the sinograms associated with these slices is incremented. The increment is applied to the same 2D location in each of the sinograms. The operation of multi-slice rebinning may be viewed as a "backprojection" of the data in the axial direction, which should be followed by an axial filtering operation.

II. SINGLE-SLICE AND MULTI-SLICE REBINNING

We denote by $I(z)$ the index of the slice containing the point at axial coordinate z. For the reconstructed slice at index $I(z)$ there is a corresponding sinogram, denoted by $sino(r, \theta, I(z))$, that is input to the reconstruction algorithm (where r and θ are the conventional indexes for 2D sinograms). For a point source (x', y', z'), we would like the contents of the array $sino(r, \theta, I(z'))$ to lead to reconstruction of an undistorted point image for the slice at index $I(z')$. For the "off z'" slices at indexes I_0, where $I_0 \neq I(z')$, we would like to have $sino(r, \theta, I_0) = 0$, so that the point source does not contribute to the reconstructed values in these slices. The simplest way to obtain a set of sinograms having these desirable properties is to make the acceptance angle very

small, so that the only coincidence lines that are accepted are those confined to a single slice of the volume. Of course, oblique lines traversing more than one slice constitute a large fraction of the coincidence data in a volumetric scanner, and so there is a need for efficient reconstruction algorithms that can utilize this data. We seek to use oblique lines and, at the same time, retain the efficiency of slice-by-slice reconstruction. Our approach involves rebinning the coincidence lines into a stack of 2D sinograms, followed by either a sinogram correction procedure in the z-direction prior to slice-by-slice reconstruction, or by an image correction procedure after slice-by-slice reconstruction.

A. Single-Slice Rebinning

In this section we describe the method of single-slice rebinning used by the UGM scanner. The description of single-slice rebinning given here is not the most direct one possible, but it is one that builds a foundation for the description of multi-slice rebinning in the next sub-section.

Let (d_1, z_1) and (d_2, z_2) be the detector coordinates resulting from coincident detection of a collinear pair of gamma rays, as shown in Fig. 1. The line from (d_1, z_1) to (d_2, z_2) is projected onto the transverse plane $z = 0$, where we determine the (r, θ) parameters of the projected line and we determine the point half-way along the projected line. For the half-way point on the projected line, we determine the z-coordinate on the original line that projects to this point. We denote this z-coordinate by $\bar{z}$, and it is easy to see that $\bar{z} = (z_1 + z_2)/2$. Let $I(\bar{z})$ denote the index of the slice containing $\bar{z}$. We denote the increment for a location in the sinogram by $incr$, and for single-slice rebinning we set $incr = 1$. Then for each coincindence line we determine r, θ and $\bar{z}$ as described above and add $incr$ to $sino(r, \theta, I(\bar{z}))$.

B. Multi-Slice Rebinning

The first part of the procedure is the same as that of single-slice rebinning. We first project the coincidence line onto the $z = 0$ plane and find r and θ for the projected line. Instead of considering just the point half-way along the projected line, we now consider the interval of length s (the choice of this parameter is discussed below) on the projected line, centered half-way along it. We then "inverse project" this interval back to the original coincidence line to determine the z-coordinates on the original line of the points that project to the ends of the interval of length s in the $z = 0$ plane. We denote these z-coordinates on the coincidence line by zlo and zhi. We denote by t the length of the projected line across the hexagon between the two detectors, i.e., t is the length of the line from detector coordinates $(d_1, 0)$ to $(d_2, 0)$. We find that

$$zlo = \bar{z} - (s/2)|z_2 - z_1|/t,$$

and

$$zhi = \bar{z} + (s/2)|z_2 - z_1|/t.$$

In multi-slice rebinning, we increment the sinograms $sino(r, \theta, i)$ for each slice i between $I(zlo)$ and $I(zhi)$. For a given coincidence line, the same increment is given to all slices in this range, but the increment is different for different coincidence lines, depending on the number of sinograms to be incremented. We make the increment inversely proportional to the number of sinograms incremented, i.e.,

$$incr = \frac{maxincr}{I(zhi) - I(zlo) + 1}.$$

In our present implementation, sinograms and increments are represented by integers, and we set $maxincr = 64$. After all coincidence lines have been rebinned, we apply a normalization factor so that the total number of counts in the stack of sinograms is equal to the number of events rebinned. For $s = 0$ we get $zlo = zhi$ and the same result as single-slice rebinning. In order to see how s should be chosen for multi-slice rebinning, consider a point (x', y', z') for which $\sqrt{x'^2 + y'^2} < s/2$, i.e., the distance of the point from the z axis is less than $s/2$. From the geometry, we see that every coincidence line through this point results in an increment to the sinogram at slice index $I(z')$, but this is no longer the case (for oblique rays) if the point is further than $s/2$ from the z axis. In our present implementation, we set s equal to the diameter of the transverse field of view.

C. Properties of Single-Slice and Multi-Slice Rebinning

The properties of the two methods of rebinning are demonstrated in Fig. 2. This figure shows the sinograms that result from the rebinning of simulated coincidence data (with slice thickness 2 mm) for an activity distribution consisting of two small (6 mm diameter) spherical sources, one centered at $(0, 0, 0)$ and the other at $(100, 0, 0)$ mm.

The top row of sinogram frames shows a range of slices in the stack of sinograms resulting from single-slice rebinning, where the slice containing the centers of both sources (i.e., the slice $z = 0$) is at the right-hand end of the row. It is evident from the sinograms that slice-by-slice reconstruction will produce an accurate image of the source at $(0, 0, 0)$, but it will produce a distorted image of the source at $(100, 0, 0)$. For the off-center source, the sinograms are non-uniform in angle (vertical direction in Fig. 2), because the counts for some angles have been assigned to slices that do not contain the source. Reconstruction from these non-uniform sinograms will lead to images that are distorted, where the image blurring is more severe in specific directions (as illustrated in Fig. 4 for measured point-source data). For a point source, the amount of the blurring in the x, y, and z directions depends strongly on the position of the source.

The middle row of sinogram frames shows the corresponding slices resulting from multi-slice rebinning. Compared to single-slice rebinning (top row) the sinograms are much more uniform in angle, but there is strong blurring in the z direction which may be corrected by axial filtering (bottom row).

For multi-slice rebinning without filtering, the reconstructed image of a point source is reasonably localized in the x and y directions, but is spread out in the z direction (as illustrated in Fig. 4 for measured point-source data). The point image is localized in x and y because the rebinned sinograms for each z are reasonably uniform over the full range of angles θ. The spread in the z direction is largest for a point source in the central slice of the axial field of view because the range of slopes of detected coincidence lines is largest for such a point. The extent of the spread in the z direction decreases steadily as the point is moved in the z direction toward the edge of the axial field of view, until the spread becomes zero at the edge of the axial field of view, where no oblique lines are detected.

The extent of the blurring in the z direction is strongly dependent on the z coordinate of the point source. This prevents the use of the most efficient deconvolution methods for deblurring in the z direction of sinograms or reconstructed images, but the problem can be tackled by more general methods. A more fundamental problem is the dependence of the blurring function on x' and y', which arises because a line at a certain r, θ, and slope (where slope = $(z_2 - z_1)/t$) through a point in the plane $z = z'$ that is far from the z axis does not increment the same set of slices as does a line having the same r, θ and slope through $(0, 0, z')$, i.e., through another point that is in the same plane but is on the z axis. This problem can be tackled by general deblurring methods operating in image space, as described in the following section. It is, however, a fundamental problem for methods that operate in sinogram space because, in the process of rebinning, coincidence lines through many different transverse points (x', y') are accumulated in the same location (r, θ) in the sinogram. For this reason, the process for correction of the sinogram has to assume that the blurring function is the same for the different points (x', y').

III. IMAGE AND SINOGRAM FILTERING

Multi-slice rebinning of coincidence data produces a stack of sinograms, each of which may be reconstructed independently by a 2D reconstruction algorithm to produce a stack of slice images, which we call the preliminary image. The rebinning of oblique coincidence lines leads to blurring in the z direction in the sinograms, and consequently in the 3D reconstructed volume.

A. Image Filtering

We use the term "object space" and coordinates (x', y', z') to refer to the 3D space containing the unknown activity distribution, denoted by f'. We use the term "image space" and coordinates (x, y, z) to refer to the 3D space containing the reconstructed estimate of the activity distribution, denoted by f, and the preliminary image, denoted by g. We assume that the detection process is linear, so that there is a linear relationship between the coincidence data and the function f'. Since multi-slice rebinning and slice-by-slice reconstruction are linear operations, the preliminary image g can be expressed in terms of the activity distribution f' by

$$g(x, y, z) = \int\int\int f'(x', y', z')\, h(x, y, z, x', y', z')\, dx'\, dy'\, dz'$$

where h is the point-response function. More specifically, $h(x, y, z, x', y', z')$ is the reconstructed value at (x, y, z) in the preliminary image due to an isolated point source at (x', y', z'). If the blurring is negligible in the x and y directions, then $h(x, y, z, x', y', z')$ is non-zero only when $x = x'$ and $y = y'$, and the general formulation in the above equation reduces to

$$g(x, y, z) = \int f'(x, y, z')\, h'(x, y, z, z')\, dz'$$

where $h'(\xi, \eta, z, z')$ is the reconstructed value at (ξ, η, z) in the preliminary image due to an isolated point source at (ξ, η, z'). The discrete form of either of the above equations can be expressed as

$$\mathbf{g} = \mathbf{H}\,\mathbf{f}'$$

where $\mathbf{g}$ and $\mathbf{f}'$ are $N \times 1$ vectors and $\mathbf{H}$ is an $N \times N$ matrix. In the case of 3D blurring, N is the total number of elements in the volume image. In the case of blurring only in the z direction, N is the number of slices, and we have a separate system of equations for each point (x, y) in the transverse plane. We will concentrate on the case of blurring only in the z direction from now on, since the computational requirements of the filtering operation are much less than the case of 3D blurring, and the blurring due to multi-slice rebinning is mostly in the z direction, as discussed in the previous section.

Each element h of the matrix $\mathbf{H}$ can be found for a particular scanner geometry by simulating the multi-slice rebinning procedure for a point source at the corresponding position on a grid in object space. The details of our implementation are described in the following section. Since $\mathbf{g}$ and $\mathbf{H}$ are known, we now have a system of linear equations for each column of the image volume (each x and y) from which we want to obtain $\mathbf{f}$ (an estimate of the activity distribution $\mathbf{f}'$) whose elements correspond to the N slices in the column.

Methods for solving the systems of linear equations that arise in the formulation of deblurring problems are discussed in many books (e.g., [8, 9]) and survey papers (e.g., [10]). The classical linear methods for these problems produce a solution vector $\mathbf{f}$ that is a compromise between satisfying the equations and satisfying some smoothness conditions. These linear methods have the advantage that the relevant matrix inverse may be precomputed and stored, and then used as a filter for different sets of data. Non-linear methods for deblurring are iterative in nature, and generally require more computation than linear methods, but they have the advantage that positivity constraints may be imposed on the elements of the solution vector $\mathbf{f}$.

For our initial tests we have chosen a method for estimating f′ from g that is relatively simple and robust, bearing in mind that the system of linear equations will be inconsistent, due to noise and errors in g and due to imperfect assumptions in the formulation of the problem. We use an iterative deblurring procedure which is known as Gold's ratio method [8] or Chahine's relaxation method [11]. The estimate of f′ resulting from the k'th iteration of this procedure is denoted by $\mathbf{f}^{(k)}$, and the procedure is initialized by setting $\mathbf{f}^{(0)} = \mathbf{g}$. The $(k+1)$'th iteration of the algorithm $(k \geq 0)$ is given by

$$\mathbf{f}_i^{(k+1)} = \mathbf{f}_i^{(k)} \left[\frac{\mathbf{g}_i}{(\mathbf{H}\mathbf{f}^{(k)})_i} \right], \qquad i = 1, \ldots, N$$

Convergence of this algorithm at $k = K$ implies that $\mathbf{f}^{(K+1)} = \mathbf{f}^{(K)}$, so that the correction factor $[\cdot]$ in the previous equation is equal to one for all components i, which implies that $\mathbf{g} = \mathbf{H}\mathbf{f}^{(K)}$, thus indicating that $\mathbf{f}^{(K)}$ at convergence is a solution to the system of equations. The theoretical conditions for convergence of the algorithm have been investigated [8, 11]. In practice, we run the algorithm for only a few iterations, stopping well short of numerical convergence. By changing the number of iterations we can achieve different compromises between deblurring of the preliminary image and amplification of the noise.

Since no elements of the system matrix H are negative, the multiplicative nature of the correction ensures that no elements of $\mathbf{f}^{(k+1)}$ can be negative, if the elements of the data vector g are also non-negative. In order to obtain this desirable property, we use as the vector g the preliminary image with any negative values set to zero.

B. Sinogram Filtering

Multi-slice rebinning of coincidence data produces a stack of sinograms, each of which may be reconstructed independently by a 2D reconstruction algorithm to produce a stack of slice images, but the rebinning of oblique coincidence lines leads to blurring in the z direction in the sinograms, and consequently in the 3D reconstructed volume. It is shown in the section on multi-slice rebinning that a point source at (x', y', z') gives a blurring in the z-direction of the stack of sinograms that depends strongly on z' and only weakly on x' and y'. If we assume that the point-spread function depends only on z', and not on x' and y', then $h'(x, y, z, z')$ is independent of the first two arguments, and the preliminary image may be expressed in terms of the activity distribution as

$$g(x, y, z) = \int f'(x, y, z')\, h^s(z, z')\, dz'$$

where $h^s(z, z')$ is the reconstructed value at (ξ, η, z) in the preliminary image due to an isolated point source at (ξ, η, z'). We now express the image-space blurring represented by the above equation by an equivalent blurring in the stack of sinograms, with coordinates (r, θ, z). We convert from image space to sinogram space by taking projections (slice-by-slice) of both sides of the above equation. The sinogram-space result is

$$q(r, \theta, z) = \int p'(r, \theta, z')\, h^s(z, z')\, dz'$$

which is obtained as follows. On the left-hand side, the operation of slice-by-slice projection of g inverts the operation of slice-by-slice reconstruction that produced g, and therefore produces the stack of sinograms resulting from multi-slice rebinning, which we denote by q. On the right-hand side, the order of the projection integration and the blur integration may be interchanged, showing that the operation of slice-by-slice projection of the z–blurred f' is equivalent to z–blurring the slice-by-slice projection of f'. The slice-by-slice projection of f', denoted by p', may be interpreted as the stack of "ideal" sinograms, i.e., the stack of sinograms from which f' would be produced by slice-by-slice reconstruction. The assumption that the point-spread function in z depends only on z', and not on x' and y', therefore allows us to model the stack of sinograms q produced by multi-slice rebinning as the result of a blurring operator in the z direction applied to the stack of ideal sinograms p', i.e., those sinograms that would result from rebinning a large number of coincidence lines that are all perpendicular to the z axis. We wish to recover an estimate, denoted by p, of the stack of ideal sinograms.

Note that p', p, and q are analogous to f', f, and g in the previous sub-section. Discretizing the above equation for the case of N slices, we obtain

$$\mathbf{q} = \mathbf{H}^s \mathbf{p}'$$

where q and p′ are $N \times 1$ vectors (for each r and θ) and $\mathbf{H}^s$ is an $N \times N$ matrix. The elements h^s of the matrix $\mathbf{H}^s$ can be found for a specific scanner geometry by simulating the multi-slice rebinning procedure for a point source at N different z-positions. Since q and $\mathbf{H}^s$ are known, we now have a system of linear equations for each r and θ from which we want to estimate the unknown $p'(r, \theta, z)$ for each slice.

We obtain an estimate of p′ using the same iterative method that we have described for image filtering, that is

$$\mathbf{p}^{(k+1)} = \mathbf{p}^{(k)} \left[\frac{\mathbf{q}}{(\mathbf{H}^s \mathbf{p}^{(k)})} \right]$$

where, as before, this equation should be interpreted as producing the i'th component of $\mathbf{p}^{(k+1)}$ from the i'th components of the vectors $\mathbf{p}^{(k)}$, q, and $(\mathbf{H}^s\mathbf{p}^{(k)})$, and the procedure is initialized by setting $\mathbf{p}^{(0)} = \mathbf{q}$. Since no elements of the data vector q or the system matrix $\mathbf{H}^s$ are negative, the multiplicative nature of the correction ensures that no elements of $\mathbf{p}^{(k+1)}$ can be negative. The algorithm therefore has the attractive property that it automatically generates solutions that are physically meaningful, with no negative counts in the deblurred sinograms.

IV. IMPLEMENTATION OF FILTERING METHODS

We now describe our specific implementations of sinogram filtering and image filtering. The numerical values quoted in the description are for the geometry of the UGM scanner (6 detectors, 865 mm effective detector separation, 128 mm effective axial field of view) with typical choices for the rebinning and reconstruction parameters (2 mm slice thickness, 6.5 degrees axial acceptance angle, 256 mm diameter reconstruction field of view, 2 mm pixel size).

A. Sinogram Filtering

For sinogram filtering, we generate $h^s(z, z')$ for 33 values of z' spaced 2 mm apart (i.e., the slice thickness) from $z' = 0$ (central transverse slice of scanner) to $z' = 64$ mm (slice at end of axial field of view). The number of samples of z depends on the acceptance angle and on the position z' in the axial field of view. For an acceptance angle of 6.5 degrees, the total width of the spread function is 15 slices at $z' = 0$, decreasing to zero width at $z' = 64$ mm. The values of the spread function for each z' are generated by multi-slice rebinning of simulated data, as follows.

A simulated point source is placed at $(0, 0, z')$ and 10,000 lines through the point source and in the y–z plane are simulated. The lines are uniformly distributed in the angular range specified by the acceptance angle (e.g., ± 6.5 degrees around the plane $z = z'$). Each simulated line that intersects a pair of detectors is rebinned, and the accumulated total for each slice in sinogram space is stored as the spread function for this value of z'. The simulated point is then moved along the z axis through a distance equal to the slice thickness, and the multi-slice rebinning process is repeated to generate the next spread function.

After the table of spread functions has been computed, the sinogram filtering is done using the iterative method described in Section III-B. For each transverse location (r, θ) in the stack of sinograms there is an axial column of length N (number of slices). The sinogram values in this axial column are selected as the elements of the vector $\mathbf{q}$, and the iterative method to estimate $\mathbf{p}'$ is initialized by setting $\mathbf{p}^{(0)} = \mathbf{q}$. After K iterations (typically 2 – 5), the vector $\mathbf{p}^{(K)}$ is stored in the axial column for this (r, θ), and the process is repeated for the next (r, θ) column in the stack of sinograms.

B. Image Filtering

For image filtering, we generate $h^i(x, y, z, z')$ for 33 values of z' spaced 2 mm apart (i.e., the slice thickness) from $z' = 0$ (central transverse slice of scanner) to $z' = 64$ mm (slice at end of axial field of view). For each value of z' we generate $h^i(x, y, z, z')$ for 49 samples of x and y on a 7×7 grid with a spacing of 20 mm, so that the grid extends from 0 to 120 mm in the x and y directions. The sample spacing in the x and y directions is larger than that in the z' direction, because the rate of variation of the function h^i is much greater in the z' direction than it is in the x and y directions. The number of samples of z depends on the acceptance angle and on the position (x, y, z'). The values of the spread function for each position are generated by multi-slice rebinning of simulated data, as follows.

A simulated point source is placed at (x, y, z') and lines through the point source are simulated. The lines are uniformly distributed in the angular range specified by the acceptance angle (e.g. ± 6.5 degrees around the plane $z = z'$) and in the angular range 0 to 180 degrees for the projection of the line onto the transverse plane. Each simulated line that intersects a pair of detectors is rebinned, and the accumulated total for each slice in sinogram space is stored as the spread function for this (x, y, z'). The simulated point is then moved to the next grid point, and the multi-slice rebinning process is repeated to generate the next spread function. We presently simulate lines for 192×256 angles (transverse $\times$ axial) for each of the $7 \times 7 \times 33 = 1617$ positions of the point source. These positions at which the spread function is computed are distributed over the image-space octant for which $x \geq 0, y \geq 0, z \geq 0$. When the blurring function h^i is needed for some arbitrary (x, y, z), the precomputed spread function at the position nearest to $(|x|, |y|, |z|)$ is used.

Examples of the point-spread function h^i are shown in Fig. 3 for points on the z' axis. Figure 3 shows clearly the decreasing height and width of the axial spread function, due to the decreasing axial acceptance angle, as the simulated point source is moved along the z' axis. The filtering process compensates the data for the relative height of the h^i functions, so the standard axial normalization is performed automatically, together with the axial deblurring. Other plots (not included here) for points at various x' and z' support the approximation that the spread function is nearly constant in the transverse direction, but changes rapidly in the z direction.

The image filtering is done using the iterative method described in Section III-A. The method is applied independently to each axial column of the image volume, in a similar manner to the implementation of sinogram filtering that is described in the previous sub-section. In future work we intend to investigate implementations of image filtering that employ some form of coupling between the corrections applied to neighboring columns.

Image filtering is more general than sinogram filtering, since our derivation of sinogram filtering is based on the assumption that the spread function for a point source at (x', y', z') is independent of x' and y'. On the other hand, this assumption means that only a few different spread functions are needed for sinogram filtering, so much less computation is required to produce the table of spread functions. Once the tables of spread functions have been produced for the respective methods, our implementation of sinogram filtering takes approximately four times as long as image filtering because of the relative sizes of the arrays involved. The sinogram array for each slice is 192 angles $\times$ 256 rays, whereas the reconstructed image for each slice is a circular

region of diameter 128 pixels. An image filtering operation of 5 iterations on a volume image of 63 slices takes less than 3 minutes with a non-optimized program on a Sun Microsystems SparcStation 330 (using a precomputed table of spread functions).

V. EXPERIMENTAL RESULTS

We show the results of an experiment using measured point-source data collected in list mode and rebinned off-line with slice thickness 2 mm. The point was positioned in the central transverse plane of the scanner at 100 mm from the scanner axis. Figure 4 shows transverse slices of the reconstructed volume after single-slice rebinning (top row), multi-slice rebinning with no filtering (second row), multi-slice rebinning with sinogram filtering (third row) and multi-slice rebinning with image filtering (bottom row). The image reconstructed after single-slice rebinning shows non-uniform blurring in the transverse slice containing the point, and considerable leakage of counts into adjacent slices. The first of these problems is greatly reduced by multi-slice rebinning and the second problem is greatly reduced by sinogram filtering or by image filtering. Figures 5, 6, and 7 show profiles in the x, y, and z directions through the reconstructed point (for volume images having approximately the same total number of positive counts). Note that the parameters chosen for the convolution–backprojection reconstruction algorithm caused significant smoothing in the transverse direction, so these results do not indicate the intrinsic resolution of the scanner.

VI. CONCLUSION

We have described the theoretical basis and a practical implementation of a method for 3D reconstruction using multi-slice rebinning and axial filtering. The filtering operation has been formulated in a general way, but an implementation of the general 3D filter has not been attempted. Two simplified versions of the general filtering operation, based on different assumptions about the nature of the point-response function, have been described and implemented. Preliminary results indicate that the assumptions are justified and that spatially varying filtering in the z direction, combined with spatially invariant filtering in the x–y directions, provides accurate 3D reconstructions with acceptable computational requirements.

ACKNOWLEDGMENTS

Multi-slice rebinning was first proposed in our research group by Dr. Caesar E. Ordonez (now with Dept. of Radiology, University of Chicago) and we acknowledge his contribution to the preliminary ideas that led to the work reported here. The major part of this work was done while Dr. Lewitt was with UGM Medical Systems on sabbatical leave from the University of Pennsylvania. We are grateful to Michael J. Pustie for assistance with the UGM software, and to Paul E. Kinahan for useful discussions. We acknowledge the partial support of the following grants: CA54356, HL28438, CA52342, DE-FG02–88ER60642.

REFERENCES

[1] J. S. Karp, G. Muehllehner, D. A. Mankoff, C. E. Ordonez, J. M. Ollinger, M. E. Daube-Witherspoon, A. Haigh, and D. Beerbohm, "Continuous-slice PENN-PET: A positron tomograph with volume imaging capability," *J. Nucl. Med.*, vol. 31, pp. 617–627, 1990.

[2] J. S. Karp, P. E. Kinahan, and D. A. Mankoff, "Positron emission tomography with a large axial acceptance angle: signal-to-noise considerations," *IEEE Trans. Med. Imaging*, vol. 10, pp. 249–255, 1991.

[3] J. S. Karp, P. E. Kinahan, P. J. Countryman, and G. Muehllehner, "Effect of increased axial field-of-view on the performance of volume PET scanners," *Conf. Record 1991 IEEE Nuclear Science Symposium* (this volume), 1991.

[4] M. E. Daube-Witherspoon and G. Muehllehner. "Treatment of axial data in three-dimensional PET," *J. Nucl. Med.*, vol. 28, pp. 1717–1724, 1987.

[5] P. E. Kinahan and J. G. Rogers, "Analytic 3D image reconstruction using all detected events," *IEEE Trans. Nucl. Sci.*, vol. 36, pp. 964–968, 1989.

[6] M. Defrise, D. W. Townsend, and A. Geissbuhler, "Implementation of three-dimensional image reconstruction for multi-ring tomographs," *Phys. Med. Biol.*, vol. 35, pp. 1361–1372, 1990.

[7] S. R. Cherry, M. Dahlbom, and E. J. Hoffman, "3D PET using a conventional multislice tomograph without septa," *J. Comput. Assist. Tomogr.*, vol. 15, pp. 655–668, 1991.

[8] P. A. Jansson, *Deconvolution With Applications in Spectroscopy*. Orlando, FL: Academic Press, 1984.

[9] S. Twomey, *Introduction to the Mathematics of Inversion in Remote Sensing and Indirect Measurements*. Amsterdam: Elsevier, 1977.

[10] B. R. Frieden, "Image enhancement and restoration," Chapter 5 in: *Picture Processing and Digital Filtering*, T. S. Huang, Ed. Berlin: Springer-Verlag, 1979, pp. 177–248.

[11] W. P. Chu, "Convergence of Chahine's nonlinear relaxation inversion method used for limb viewing remote sensing," *Appl. Opt.*, vol. 24, pp. 445–447, 1985.

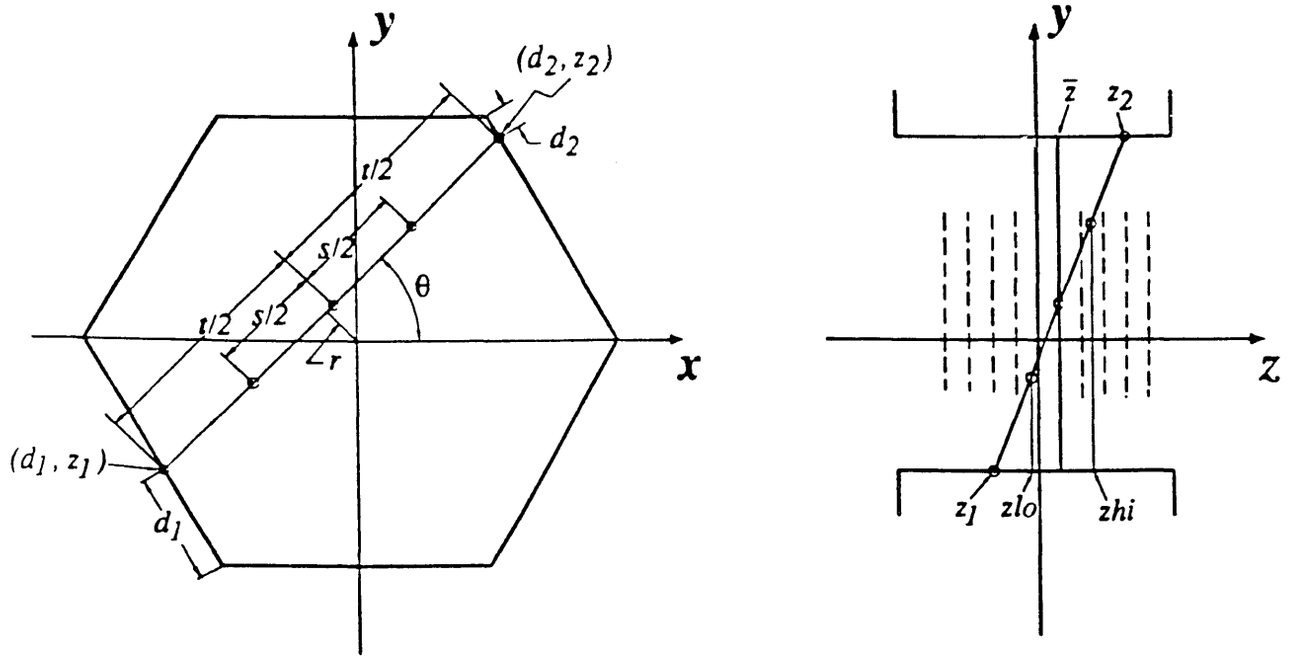

Fig. 1. Transverse and axial geometry for multi-slice rebinning.

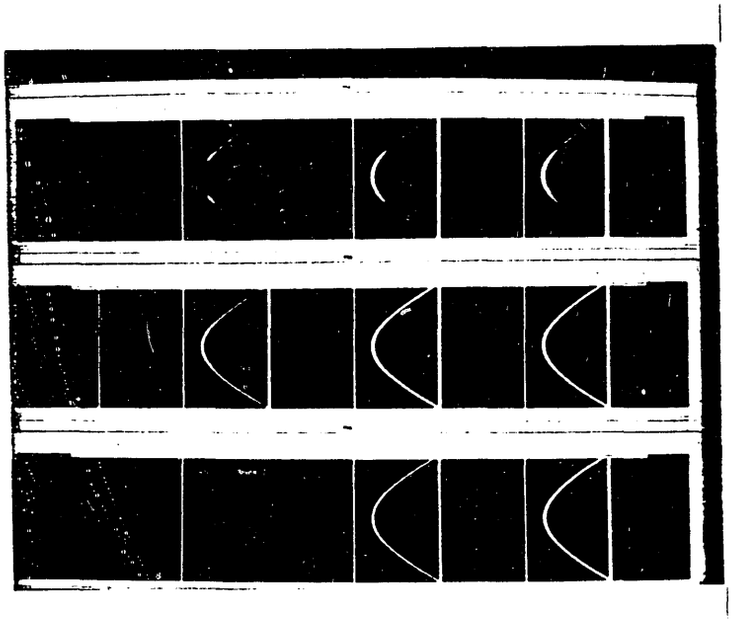

Fig. 2. Sinograms demonstrating properties of single-slice rebinning (top row), multi-slice rebinning (middle row), and multi-slice rebinning with axial filtering (bottom row).

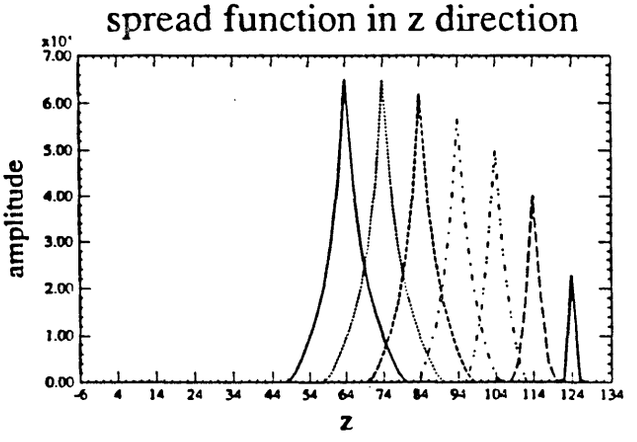

Fig. 3. Spread functions for 7 points on z axis, from z=0 (axial position 64 on plot) to z=60 mm (axial position 124), in steps of 10 mm.

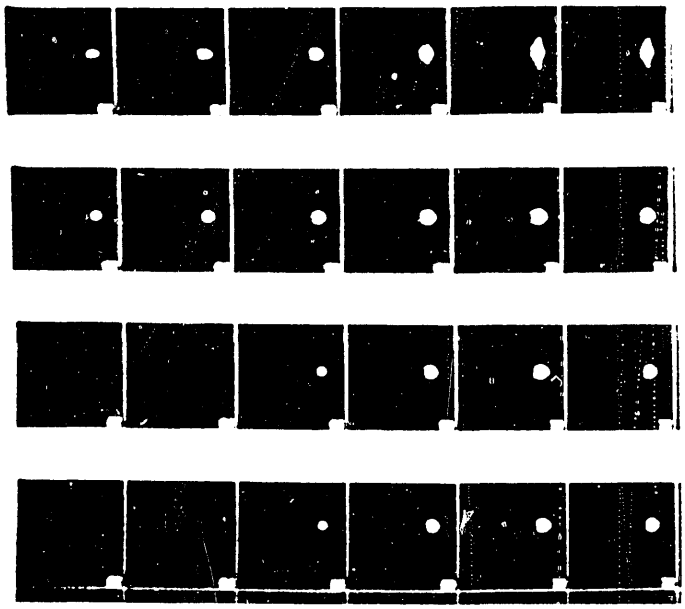

Fig. 4. Transverse slices of volume images reconstructed from measured data for a point source at (approximately) x=100 mm, y=2 mm, z=6 mm (i.e., axial position 6-4+6 on z-profile shown in Fig. 7).
Top row: single-slice rebinning

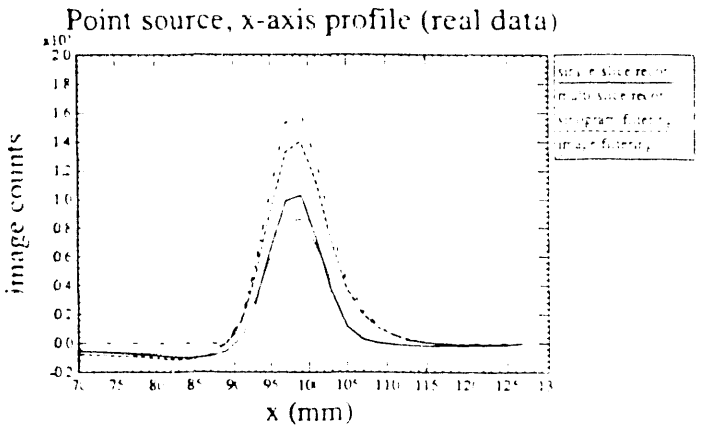

Fig. 5. Profile through point: x direction.

Second row: multi-slice rebinning with no filtering
Third row: multi-slice rebinning with sinogram filtering
Bottom row: multi-slice rebinning with image filtering

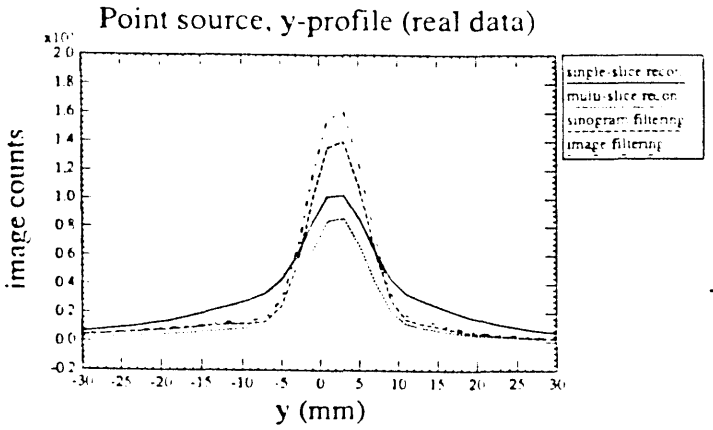

Fig. 6. Profile through point: y direction.

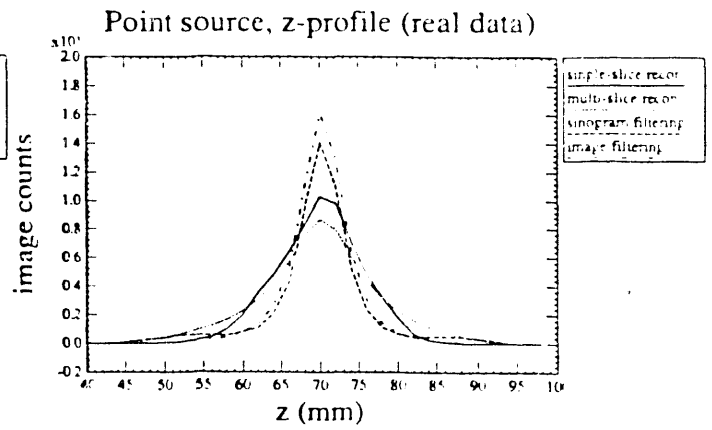

Fig. 7. Profile through point: z direction.

END

DATE
FILMED
2 12092

I